Formation of dissipative structures in a three-dimensional electro-thermo-convective flow

Kang Luo,[1,2] Xue-Lin Gao,[1,2] Xue-Rao He,[3] Hong-Liang Yi,[1,2,*] and Jian Wu[1,2]

[1]*School of Energy Science and Engineering, Harbin Institute of Technology, Harbin 150001, People's Republic of China*

[2]*Key Laboratory of Aerospace Thermophysics, Harbin Institute of Technology, Harbin 150001, People's Republic of China*

[3]*Department of Mechanical Engineering, National University of Singapore, 9 Engineering Drive 1, 117575, Singapore*

(Received 11 January 2022; accepted 28 March 2022; published 11 April 2022)

Direct numerical simulations and linear stability analysis are performed to study the three-dimensional electro-thermo-convective (ETC) flow between two parallel plates under a simultaneously applied temperature difference and voltage. Entropy generation analysis and hexagonal pattern analysis are used to illustrate the transient evolution and stationary dissipative structures of an ETC flow. Numerical simulations with a large computational domain are first performed to reproduce the experimentally observed motion pattern under strong unipolar charge injection. The results show that an infinitesimal random perturbation first grows into a rolls pattern, then partially breaks up into polygons, and finally evolves into hexagons after a long period of transition. Linear stability analysis is conducted to obtain the stability criteria (electric Rayleigh number T_c and Rayleigh number Ra_c) and the critical wave number (k_c) of the ETC flow, and these critical values are found to be consistent with the numerically obtained ones. In addition, it is found that the basic features of the numerically obtained ETC hexagonal flow pattern agree with those of the analytically derived cell pattern. By entropy generation analysis of ETC in a periodic region, it is found that the formation of the rolls pattern has a larger total entropy generation and a larger mean-square temperature gradient than the hexagon pattern, which means that the rolls pattern is more stable than the hexagon under this specific simulation condition.

DOI: 10.1103/PhysRevFluids.7.043701

I. INTRODUCTION

A dissipative structure is formed in an open system far from the equilibrium state by constantly exchanging energy with the outside world. When the externally applied energy reaches a certain threshold, the system spontaneously transforms from its original disordered state into a spatially and temporally ordered state, thereby forming a new, stable, and ordered structure [1]. Bénard's thermal convection (RBC) [2] and electroconvection (EC) [3] are two well-known examples. In these cases, energy flux flows across a fluid layer subjected to a temperature difference or an electric potential difference, respectively. The input energy thus generates a periodic dissipative convective structure, usually with two-dimensional (2D) rolls or three-dimensional (3D) hexagonal cells [4–8].

The study of EC is in many ways analogous to that of RBC due to the physical and phenomenal similarities between the two. However, there are also clear differences between the two, such as the linear energy equation in RBC compared to the nonlinear charge conservation equation in EC [9],

*Corresponding author: yihongliang@hit.edu.cn

that heat is transferred by diffusion in a hydrostatic state while charges are transported via drift and diffusion mechanisms [10], or that there is a supercritical pitchfork bifurcation in the onset of RBC in a Boussinesq fluid [4] but a subcritical bifurcation in EC under unipolar injection (featured by a linear stability criterion, a nonlinear one, and a hysteresis loop between them [11,12]). Compared to the widespread attention of RBC problems, the EC instability is still not well understood especially in three dimensions.

One interesting problem to consider is the combined effects of an electric field and a thermal gradient simultaneously applied to a horizontal dielectric liquid layer, in which case the interactions of the RBC and EC instabilities will lead to electro-thermo-convective (ETC) instabilities. One particular reason for interest in this problem is promising applications in heat transfer augmentation and fluid control [13–21], especially in microdevices [22] or microgravity environment [23]. A lot of attention has been drawn to this active field, from the perspectives of stability analysis [3,7,24,25], experimental study [16,17,26], and numerical simulations [27–30]. Linear and nonlinear stability analysis has been extensively used since the 1980s to predict the stability criteria associated with the plate-plate configuration [31]. The effects of the injection strength [32], temperature-dependent parameters [32], the residual conductivity [33], the cross-flow [24,34], and the non-Newtonian fluid effect [35] on the stability criteria have been investigated. Experimental studies have also been performed to evaluate the effect of electro-convection on heat transfer, for both single-phase and two-phase fluid systems [14,15,36–39] under different electrode configurations, and the results have confirmed that ion injection can serve as an effective technique with which to actively augment heat transfer. Furthermore, direct numerical simulations are an important way to gain some fundamental insights into complex ETC phenomena [27–30]. Among the various numerical methods, the finite volume method (FVM) [6] and lattice Boltzmann method [28,40] have been relatively popular in recent years.

Although ETC phenomena have been extensively studied using different methods, most of this work has been limited to two-dimensional models. Kourmatzis *et al.* [10] conducted a three-dimensional simulation of EC between two plates using the FLUENT software, focusing mainly on the fully turbulent regime at high electric Reynolds numbers. Luo *et al.* [29] developed a lattice Boltzmann code for three-dimensional EC and found that a hexagonal cell with a central region empty of charge and central downward flow is preferred in symmetric systems under a random initial disturbance or a special hexagonal perturbation. Guan *et al.* [41] investigated three-dimensional EC with a cross flow and found that the interactions between the cross flow and electro-convective vortices lead to the suppression and elimination of structures with velocity components in the direction of the cross flow. However, few numerical studies have been devoted to the three-dimensional ETC problem.

It should be noted that hexagonal patterns are observed in experiments with a very large aspect ratio $\Gamma = L/H \geqslant 25$ [3] (where L is the diameter of the electrode and H is the distance between electrodes). But previous 3D numerical simulations were conducted within a small computational domain [8,41]. A limited domain size naturally restricts the development of some modes of the perturbation and the flow may not tend to a fully developed state as in real situations. In this work, we make use of a computation with a large domain ($\Gamma = 20$) with the help of high-performance clusters.

The main objectives of this work are threefold: (1) to conduct a large-domain computation to reproduce experimentally observed motion patterns under strong unipolar charge injection, (2) to investigate the onset of instability and a stationary 3D dissipative structure in an electro-thermo-convective flow, (3) to introduce entropy generation analysis into the ETC problem, and explain why some specific cell patterns are preferred.

II. MATHEMATICAL FORMULATION

A. Physical problem and governing equations

As shown in Fig. 1, a dielectric fluid layer of thickness H is enclosed between two planar electrodes of area $L_x \times L_y$ normal to the z axis. The aspect ratios of the configuration are defined as

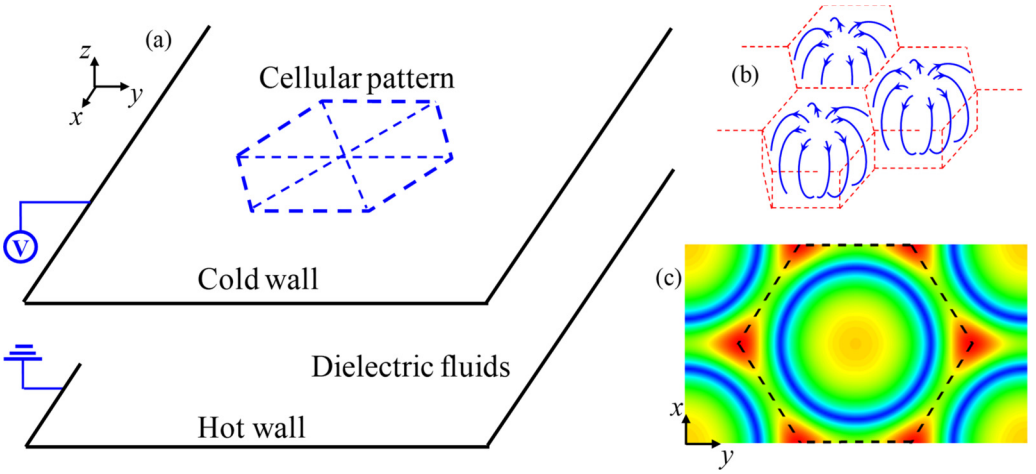

FIG. 1. A schematic diagram of (a) the physical model and (b) the hexagonal pattern; (c) the velocity magnitude at the slice $z = H/2$ in a periodic domain, with an auxiliary dashed line to highlight the hexagonal pattern.

$\Gamma_x = L_x/H$ and $\Gamma_y = L_y/H$. An electric potential difference $\Delta\phi$ and a temperature difference $\Delta\theta$ are simultaneously applied. Heating from the bottom and charge injection from the top are assumed to form a centrally upward flow (also called l cells in Ref. [4]).

Considering an incompressible, Newtonian, and linear isotropic dielectric fluid, under the assumptions of the Boussinesq approximation and unipolar charge injection, ignoring magnetic effects and Joule heat, and taking $K\Delta\phi/H$, $H^2/K\Delta\phi$, $\Delta\phi$, $\Delta\theta$, and q_0 to be the velocity, time, electric potential, temperature, and charge density scales, respectively, the dimensionless mathematical formulations are given as [42,43]

$$\nabla \cdot \mathbf{u} = 0, \tag{1}$$

$$\frac{\partial \mathbf{u}}{\partial t} + (\mathbf{u}\cdot\nabla)\mathbf{u} = -\nabla\hat{p} + \frac{M^2}{T}\nabla^2\mathbf{u} + CM^2 q\mathbf{E} + \frac{M^4\mathrm{Ra}}{T^2\mathrm{Pr}}\theta\mathbf{e}_z, \tag{2}$$

$$\nabla^2\phi = -Cq,\ \mathbf{E} = -\nabla\phi, \tag{3}$$

$$\frac{\partial q}{\partial t} + \nabla\cdot(\mathbf{E}q + \mathbf{u}q) = \alpha\nabla^2 q, \tag{4}$$

$$\frac{\partial \theta}{\partial t} + \mathbf{u}\cdot\nabla\theta = \frac{M^2}{T\mathrm{Pr}}\nabla^2\theta, \tag{5}$$

where $\mathbf{u} = [u, v, w]$ and $\mathbf{E} = [E_x, E_y, E_z]$ are the fluid velocity and electric field, respectively. The scalars ρ, $\hat{p}$, ϕ, q, and θ denote the fluid density, a modified pressure [43], the electric potential, the charge density, and the temperature. The system is governed by the following six dimensionless parameters (From left to right: Rayleigh number, electric Rayleigh number, Prandtl number, injection strength, non-dimensional mobility and non-dimensional charge diffusion coefficient):

$$\mathrm{Ra} = \frac{g\beta\Delta\theta H^3}{\nu\chi},\quad T = \frac{\varepsilon\Delta\phi_0}{\mu K},\quad \mathrm{Pr} = \frac{\nu}{\chi},\quad C = \frac{q_0 H^2}{\varepsilon\Delta\phi_0},\quad M = \frac{1}{K}\left(\frac{\varepsilon}{\rho_0}\right)^{1/2},\quad \alpha = \frac{D}{K\Delta\phi_0}. \tag{6}$$

The symbols μ, β, ε, K, D, χ, in turn, stand for the dynamic viscosity, the coefficient of volumetric expansion, the electrical permittivity, the ionic mobility, the charge-diffusion coefficient, and the thermal diffusivity [6].

B. Direct numerical simulation using the lattice Boltzmann method

Direct numerical simulations are a useful way to gain fundamental insights into complex ETC phenomena. By integrating the thermal and electrical parts of a code with general CFD solvers, such as the LBM, FVM, or Nek5000, we can build up a platform for ETC simulations. Among the CFD solvers, the LBM is a relatively simple numerical tool for the study of multiphysics coupling problems such as the present ETC problem. In our previous work, we developed a unified LBM for 2D ETC scenarios [28,44] and this model has been extended by a series of follow-up papers [45–48]. Therefore, here we just provide the fundamental equations for the LBM and refer the reader to the aforementioned references for further information.

Four consistent lattice Boltzmann equations (LBEs) corresponding to the macroscopic equations for a flow field [Eqs. (1) and (2)], a temperature field [Eq. (5)], an electric potential field [Eq. (3)], and a charge density distribution [Eq. (4)], are respectively given as follows:

$$f_j(\mathbf{x}+\mathbf{c}_j\Delta t, t+\Delta t) - f_j(\mathbf{x},t) = -\frac{1}{\tau_v}\left[f_j(\mathbf{x},t) - f_j^{\mathrm{eq}}(\mathbf{x},t)\right] + \Delta t \times F_j, \tag{7}$$

$$l_j(\mathbf{x}+\mathbf{c}_j\Delta t, t+\Delta t) - l_j(\mathbf{x},t) = -\frac{1}{\tau_\theta}\left[l_j(\mathbf{x},t) - l_j^{\mathrm{eq}}(\mathbf{x},t)\right], \tag{8}$$

$$g_j(\mathbf{x}+\mathbf{c}_j\Delta t, t+\Delta t) - g_j(\mathbf{x},t) = -\frac{1}{\tau_\phi}\left[g_j(\mathbf{x},t) - g_j^{\mathrm{eq}}(\mathbf{x},t)\right] + \Delta t \times S_j, \tag{9}$$

$$h_j(\mathbf{x}+\mathbf{c}_j\Delta t, t+\Delta t) - h_j(\mathbf{x},t) = -\frac{1}{\tau_q}\left[h_j(\mathbf{x},t) - h_j^{\mathrm{eq}}(\mathbf{x},t)\right], \tag{10}$$

where f_j, l_j, g_j, and h_j stand for the distribution functions of the flow field, temperature field, electric potential, and charge density, respectively. The consistent velocity discretization schemes of the D2Q9 and D3Q19 models (D stands for dimensions and Q for the number of directions [49]) models are adopted for all fields in two dimensions and three dimensions, respectively.

The equilibrium distributions f_j^{eq}, l_j^{eq}, g_j^{eq}, and h_j^{eq} can be calculated using a simplified Maxwell's distribution and take the following unified form:

$$f_j^{\mathrm{eq}} = \rho\omega_j\left(1 + \frac{\mathbf{c}_j\cdot\mathbf{u}}{c_s^2} + \frac{(\mathbf{c}_j\cdot\mathbf{u})^2}{2c_s^4} - \frac{\mathbf{u}\cdot\mathbf{u}}{2c_s^2}\right), \tag{11}$$

$$l_j^{\mathrm{eq}} = \theta\omega_j\left(1 + \frac{\mathbf{c}_j\cdot\mathbf{u}}{c_s^2} + \frac{(\mathbf{c}_j\cdot\mathbf{u})^2}{2c_s^4} - \frac{\mathbf{u}\cdot\mathbf{u}}{2c_s^2}\right), \tag{12}$$

$$g_j^{\mathrm{eq}}(\mathbf{x},t) = \omega_j\phi, \tag{13}$$

$$h_j^{\mathrm{eq}}(\mathbf{x},t) = q\omega_j\left\{1 + \frac{\mathbf{c}_j(K\mathbf{E}+\mathbf{u})}{c_s^2} + \frac{[\mathbf{c}_j(K\mathbf{E}+\mathbf{u})]^2 - c_s^2(K\mathbf{E}+\mathbf{u})^2}{2c_s^4}\right\}, \tag{14}$$

in which the lattice sound speed $c_s = c/\sqrt{3}$. The relaxation times τ in Eqs. (7)–(10) are defined as

$$\tau_v = \frac{3\nu}{c^2\Delta t} + \frac{1}{2}, \quad \tau_\theta = \frac{3\chi}{c^2\Delta t} + \frac{1}{2}, \quad \tau_\phi = \frac{3\gamma}{c^2\Delta t} + \frac{1}{2}, \quad \tau_q = \frac{3D}{c^2\Delta t} + \frac{1}{2}. \tag{15}$$

In addition, the force term in Eq. (7) and the source term in Eq. (9) are formulated through the split-forcing scheme,

$$F_j = \omega_j\left(1 - \frac{1}{2\tau_v}\right)\frac{\mathbf{c}_j[q\mathbf{E}+\rho\mathbf{g}\beta(\theta-\theta_{\mathrm{ref}})]}{c_s^2}, \tag{16}$$

$$S_j = \omega_j\gamma q/\varepsilon. \tag{17}$$

After the evolution process, the macroscopic quantities are obtained from

$$\rho = \sum_j f_j, \quad \rho\mathbf{u} = \sum_j \mathbf{c}_j f_j + \frac{\Delta t}{2} q\mathbf{E}, \quad \theta = \sum_j l_j, \quad \phi = \sum_j g_j,$$
$$\mathbf{E} = \frac{1}{\tau_\phi c_s^2 \Delta t} \sum_j \mathbf{c}_j g_j, \quad q = \sum_j h_j. \tag{18}$$

It should be noted that the macroscopic equations (1)–(4) can be recovered from the LBEs in Eqs. (7)–(10) using the Chapman-Enskog expansion as in Ref. [28].

C. Entropy generation in an ETC flow

The thermal gradient and electric potential between the two planar electrodes drive the fluid in a nonequilibrium state which causes entropy generation in the system. As derived by Castellanos [50], the equation of local entropy generation in nonpolar fluids is given by

$$\dot{S} = \mathbf{J}_o' \cdot \nabla\left(\frac{1}{\theta_0}\right) + \frac{\Phi}{\theta_0} + \mathbf{J}' \cdot \left(\frac{\mathbf{E}}{\theta_0}\right), \tag{19}$$

where θ_0 is the absolute temperature and $\mathbf{J}_o'$ is the heat flow measured by an observer comoving with an element of the fluid [50], as given by the Fourier law in Eq. (20a). $\mathbf{J}' = \mathbf{J} - q\mathbf{u}$ is the current density measured in the comoving frame of reference of the fluid element [50], expressed in Eq. (20b), and Φ is the rate at which energy is dissipated by viscosity [51], as given in Eq. (20c),

$$\mathbf{J}_0' = -\lambda \nabla\theta, \tag{20a}$$
$$\mathbf{J}' = K\mathbf{E}q - D\nabla q, \tag{20b}$$
$$\Phi = 2\mu\left[\left(\frac{\partial u}{\partial x}\right)^2 + \left(\frac{\partial v}{\partial y}\right)^2 + \left(\frac{\partial w}{\partial z}\right)^2\right] + \mu\left[\left(\frac{\partial u}{\partial y} + \frac{\partial v}{\partial x}\right)^2 + \left(\frac{\partial u}{\partial z} + \frac{\partial w}{\partial x}\right)^2 + \left(\frac{\partial v}{\partial z} + \frac{\partial w}{\partial y}\right)^2\right]. \tag{20c}$$

The three terms on the right-hand side of Eq. (19) represent local entropy generation due to heat transfer ($\dot{S}_h$), fluid friction ($\dot{S}_f$), and electric current ($\dot{S}_e$), respectively.

In addition to entropy generation, we make use of another criterion for measuring the relative stability deduced by Malkus and Veronis [52], that the stable solution has a greater mean-square gradient than any other solution. This can be expressed by the equation

$$(\bar{\beta}^2)_m > \left(\bar{\beta}_i^2\right)_m. \tag{21}$$

Here $\bar{\beta} = -\partial\bar{\theta}/\partial z$ is the mean temperature gradient with $\bar{\theta}$ being the average temperature over a horizontal plane. The subscript m is the mean of the gradient along the z direction and the index i ranges over all solutions but the one considered.

III. RESULTS AND DISCUSSION

In this section, to gain a deeper insight into the formation of cell patterns in an ETC flow, results from numerical simulations, modal stability analysis, hexagonal pattern analysis, and entropy generation analysis are presented and compared. The validation of our numerical method is conducted by a qualitative comparison with an experiment in Sec. III A and a quantitative comparison with stability analysis in Sec. III B.

A. Formation of cells pattern between two large plates: Simulation versus experiment

In order to reduce the horizontal boundary effect on pattern formation, large plates (sometimes approximated as infinite plates) are used in experimental observations of both RBC cells [3] and EC

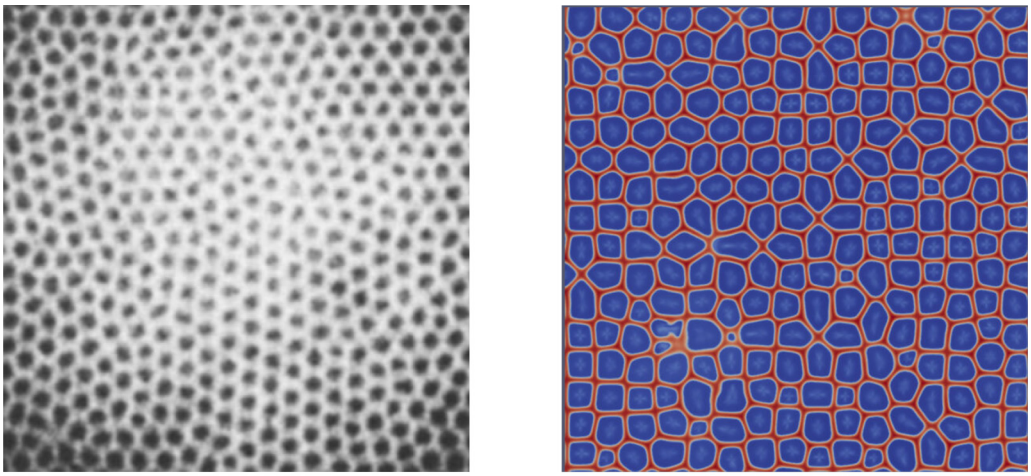

FIG. 2. A comparison between (a) Atten's classic experiment [2] (a partial domain for comparison purposes) and (b) present numerical simulation with the parameters $\Gamma_x = \Gamma_y = 20$, $T = 180$, $M = 10$, $C = 10$, and $\alpha = 10^{-3}$.

cells [2]. But this large domain is hard to numerically reproduce due to its large computation cost. Existing works are limited to small computational domains with periodic boundary conditions to obtain artificial cell flow patterns [53]. In order to get closer to the real experiment conditions, in this section, we first conduct a large domain simulation ($\Gamma_x = \Gamma_y = 20$) by embedding our thermal and electrical parts of codes into the open source framework Nek5000, with an average grid resolution of $\Delta z = 0.01$, running on a high-performance cluster with 1000 cores.

Figure 2 shows a comparison between the experimentally [2] and numerically observed cell flow patterns. The simulation was conducted under a random initial infinitesimal perturbation in the whole domain, with a free boundary condition in the wall-parallel direction, for the parameters $T = 180$, $M = 10$, $C = 10$, and $\alpha = 10^{-3}$. As shown in Fig. 2, the numerical results qualitatively agree well with the experimental data. In both figures, the fluid domain is fully filled by polygons, including quadrangles, pentagons, and hexagons. Among the hexagons, both irregular and regular shapes can be clearly observed.

To better understand the transient formation of cell patterns between two large plates, in Fig. 3, we plot the isosurfaces (top view) of the vertical velocity component w at three representative points in time. Using these figures, we can separate the whole formation process into three stages. In the first stage, the perturbations corresponding to different modes are excited in the domain, a pattern of rolls is first produced as shown in Fig. 3(a) [and is also clearly seen in Fig. 3(d), which is a zoomed-in image of 1/15 of the computational domain]. Note that the linear analysis is unable to provide information on the preferred convective platform. With the development of the flow pattern, the dominant modes may change. As seen in Fig. 3(b), the rolls pattern bifurcates into polygons, first in the upper right, and then covering the whole domain. In the last region, the flow slightly regulates itself into a more regular and stable hexagonal pattern as seen in Fig. 3(c), with a partial enlargement of the 3D picture also provided in Fig. 3(e). This self-adjustment process is extremely slow.

B. Stability criteria as obtained by linear stability analysis and LBM simulations

The formation of dissipative structures begins with infinitesimal disturbances in a stationary system. Using modal stability analysis, we can determine the most unstable disturbance and the

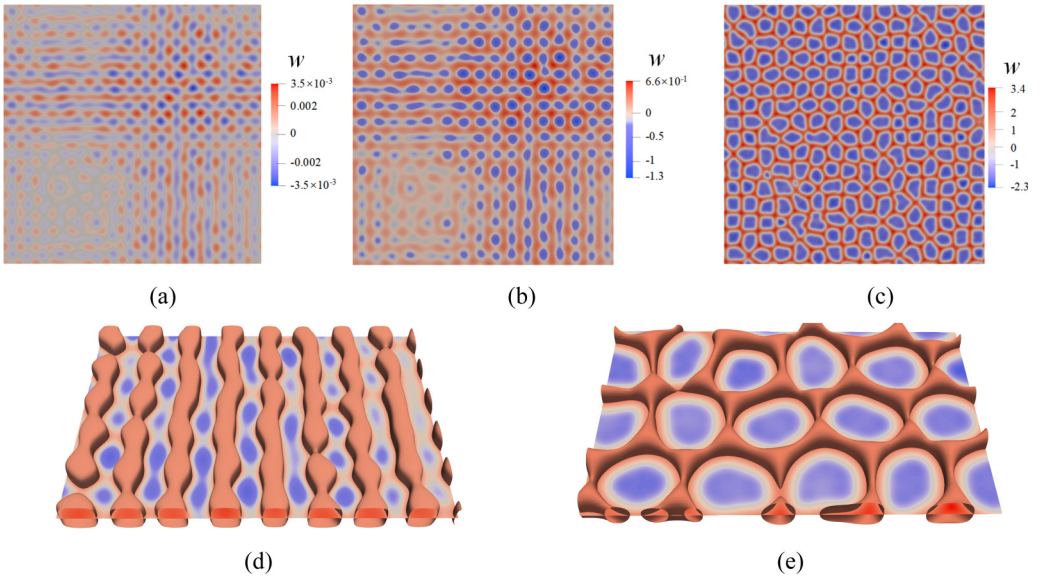

FIG. 3. A top view of the vertical velocity component w at three representative points in time: (a) $t = 16$; (b) $t = 27$; (c) $t = 38.6$. Panels (d) and (e) are zoomed-in 3D views of 1/15 of the domain of (a) and (c), respectively.

corresponding critical wave number, which may provide some guidance for the flow pattern analysis. By solving the eigenvalue problem given in Eq. (B17), we can obtain the imaginary component ω_i, which represents the growth rate of the perturbation, and then determine the stability of the system under a given wave number k and specific governing parameters.

It should be noted that the stability of the ETC flow depends on the combination of T and Ra, so in practice, we fix one parameter and seek information about the other. For example, in Figs. 4(a) and 4(b), we display spectra for an ETC flow at $T = 120$ and $T = 150$ under a fixed Ra $= 400$, respectively. It is shown that the real parts of the leading eigenvalues for the two cases are zero,

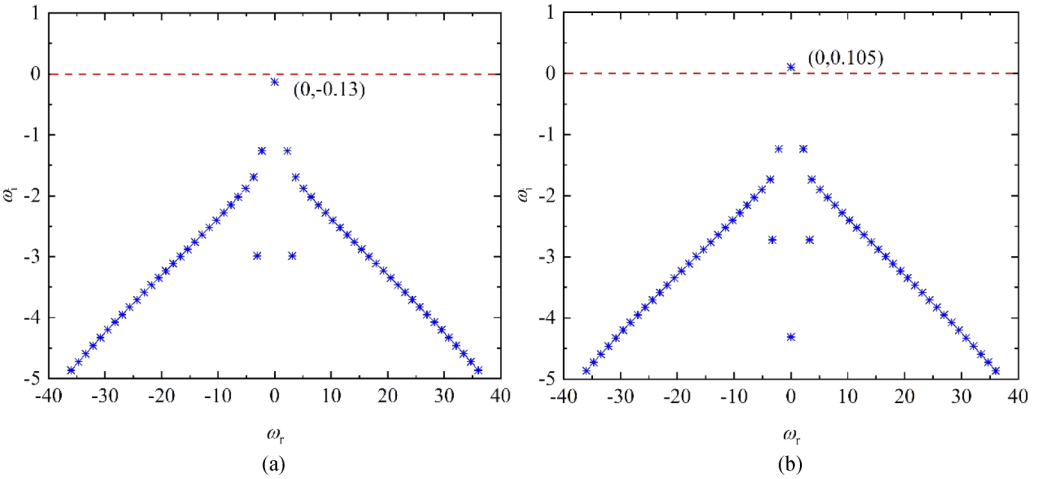

FIG. 4. Spectra for an ETHD flow between two parallel plates at $C = 10$, $M = 10$, Pr $= 10$, $\alpha = 10^{-4}$, Ra $= 400$, and $k = 4$, (a) $T = 120$; (b) $T = 150$.

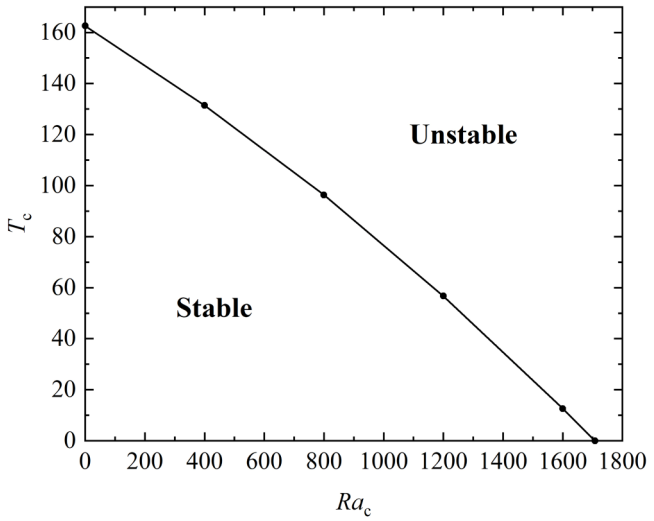

FIG. 5. The neutral stability curve in the Ra-T plane for an ETC flow between two parallel plates at $C = 10$, $M = 10$, Pr $= 10$, and $\alpha = 10^{-4}$.

which means that the perturbations decay or increase monotonically. At $T = 120$, the imaginary part of the first eigenvalue is smaller than zero, which indicates that the linear system is stable, and the decay rate of the linear perturbation is -0.13. In addition, since the largest eigenvalue lies above $\omega_i = 0$ at $T = 150$, the linear system is unstable and the growth rate is 0.105. Using this method, we can evaluate the critical k_c and T_c (the subscript c indicates critical value) at which the value of ω_i equals zero.

In the same manner, the value of T_c can be calculated for different Ra, producing the neutral stability curve for the ETC flow shown in Fig. 5. The fitted curve separates the whole domain into a stable region and an unstable one. The two ends of the stability curve (the intersections with the coordinate axes) correspond to pure RBC and pure EC scenarios, respectively. For the pure RBC case, the linear stability criterion is $\mathrm{Ra}_c = 1707.762$ with a critical wave number $k_c = 3.117$ [2], independent of Pr. For the pure EC case, the linear stability criterion strongly depends on the injection strength C but is independent of the mobility parameter M. For the case of $C = 10$ and $\alpha = 0$, the criterion and critical wave number are $T_c = 164.1$ and $k_c = 5.113$ [3], respectively.

Linear stability criteria can also be obtained in this numerical manner, by setting the driving parameters Ra and T close to the estimated linear instability threshold and examining the development of the initial perturbation. The time histories of the peak velocity $V_{\max}$ for the three different $T = 145$, 150, and 155 for Ra $= 400$ are plotted in Fig. 6(a). It is seen that all cases eventually reach a stable state of convection. As shown in Fig. 6(b), the relation between $V_{\max}$ and the time t is linear in logarithmic coordinates, which means the development of the perturbations in the velocity field at the initial stage follows an exponential law, called as growth rate [8]. The extracted growth rates for the cases $T = 145$, 150, and 155 are plotted in Fig. 6(c), then extrapolated to obtain the linear stability criterion corresponding to the zero-growth rate, finally giving $T_c = 139.1$ for Ra $= 400$. In the same manner, for a given wave number $k = 5.5$, the values of T_c at Ra $= 800$ and 1200 are calculated approximately to be 114.7 and 90.3, respectively. Repeat the steps shown in Figs. 6(a)–6(c) for different k and Ra, we can obtain the $k - T_c$ curves as presented in Fig. 6(d).

Good agreement between the numerical simulation and modal-stability analysis can be observed in Fig. 6(d). Here, the numerically predicted linear stability criteria obtained from the LBM are based on a large number of computational runs for different wave numbers $k \in (3$–$5.5)$ and Ra $=$ (400, 800, 1200). The numerically predicted values of T_c at the critical wave number k_c are 133.5,

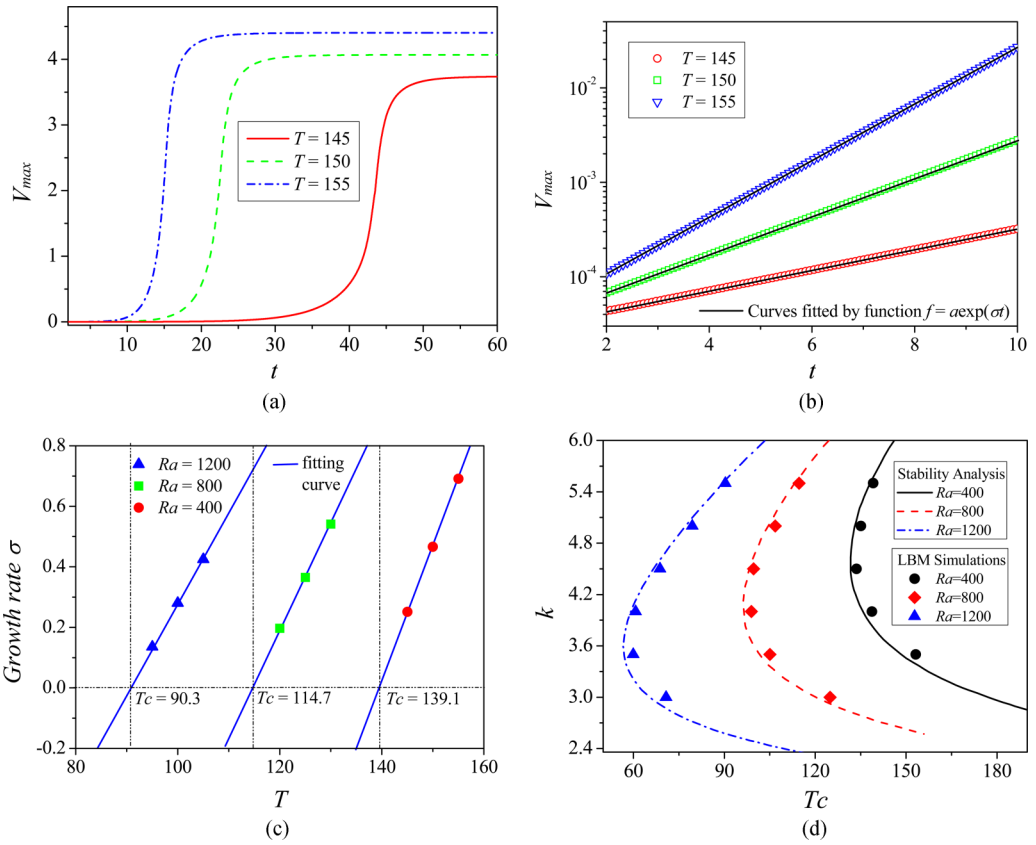

FIG. 6. Linear stability criteria for the ETC flow obtained from an LBM simulation and compared with stability analysis results: (a) time histories of the peak velocity $V_{\max}$ for $T = 145$, 150, and 155 at Ra $= 400$ and $k = 5.5$, (b) the extraction of the exponential growth stage and the fit of the growth rate, (c) the linear fitting of the growth rates for Ra $= 400$, 800, and 1200, with the intersections of the lines with the x axis giving the values of T corresponding to neutral stability, (d) a comparison between the T_c obtained from the numerical simulation and stability analysis at different wave numbers k and Ra.

99.1, and 59.5 for Ra $= 400$, 800, and 1200, respectively, close to the values obtained by stability analysis (131.1, 96.2, 56.5). The difference between the LBM simulation and stability analysis may be explained by the fact that, unlike the single wave number k used in linear stability analysis, it is hard to eliminate the higher harmonics effect in direct numerical simulation, which may affect the numerical prediction of growth rate. Moreover, a larger k corresponds to a smaller computational domain where the higher harmonics are effectively restrained, which explains the relatively large difference at smaller k but strong consistency between the LBM simulation and stability analysis at larger k.

C. Analytical solution and LBM simulation of the hexagonal pattern

For an isotropic liquid where no favored direction exists in the horizontal plane, a hexagonal pattern possesses a higher symmetry than other distributions such as squares or rectangles [2]. Hence, the flow slowly regulates itself from polygons toward a more regular hexagonal pattern. Owing to the periodicities of the flow in both the x and y directions, we can simply pick out one periodic unit to represent the flow features. Figure 7 presents a comparison between the analytical solution and the LBM simulation within one hexagonal cell. The analytical solution of w and

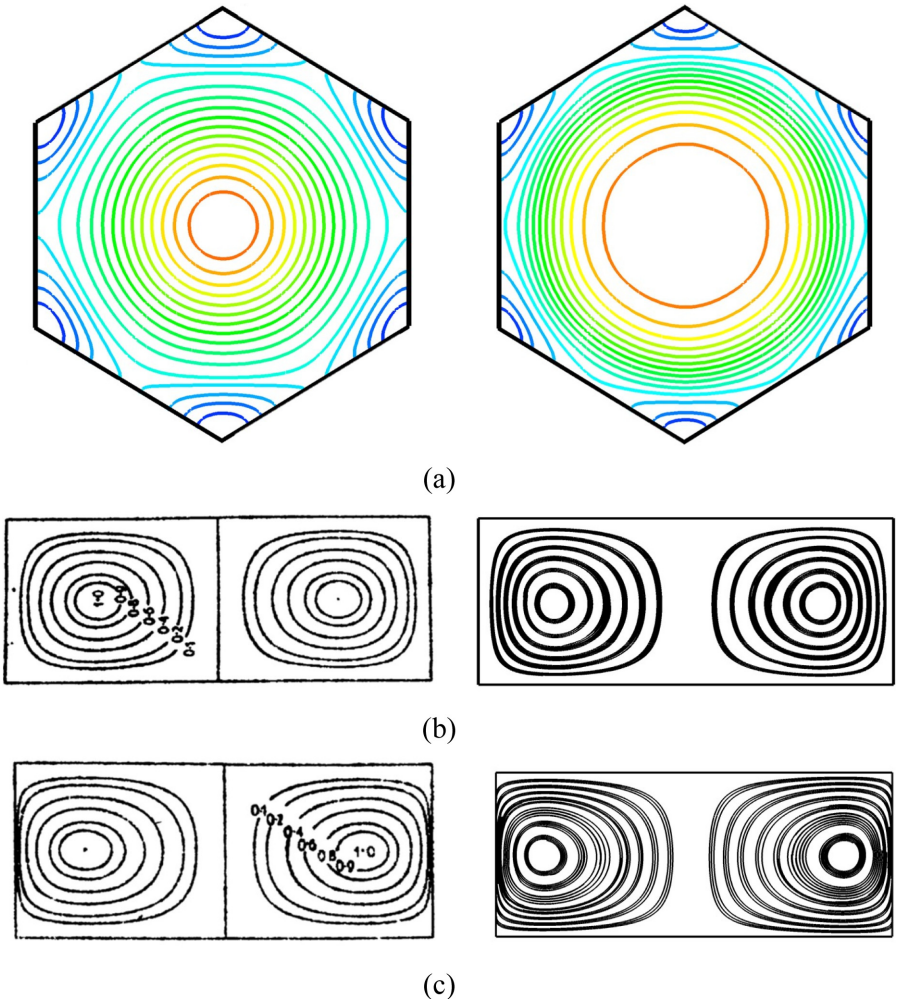

FIG. 7. A comparison between the analytical description of a hexagonal cell obtained by Chandrasekhar [2] (left) and the LBM simulation (right): (a) the vertical velocity w at slice $z = H/2$; streamlines at (b) slice $x = 0$ and (c) slice $y = 0$.

streamlines at slices $x = 0$ and $y = 0$ are expressed by Eqs. (A1), (A10), and (A11) in Appendix A, respectively. It is seen that the numerical results exhibit the basic features of a hexagonal pattern, similar to the analytical solution [2]. However, a discrepancy in the w distribution can be observed in Fig. 7(a), due to the nonlinear feature of the charge conservation equation, which causes a charge void region in the center of the hexagon and a larger velocity magnitude than in the theoretical prediction. Furthermore, the fluid ascends in the center and descends in the peripheral regions, leading to a pair of vortices in both slices $x = 0$ [Fig. 7(b)] and $y = 0$ [Fig. 7(c)].

A full view of the hexagonal pattern in one periodic unit is presented in Fig. 8. The rolls pattern is also shown for comparative analysis. The simulations are conducted based on the LBM with the size of the computational domain chosen to be $\Gamma_x = \lambda_x$ and $\Gamma_y = \lambda_y$, where $\lambda_x = 2\pi/k_x$ and $\lambda_y = 2\pi/k_y$ are the wavelengths in the streamwise and spanwise directions, respectively. As shown in Fig. 8(a), the flow shows a straight roll structure and can be viewed as an extension of 2D rolls in the x direction. Two thermal plumes, two independent charge void regions, and two pairs of counter-rotating rolls are readily seen. The counter-rotating rolls are symmetrical to each other.

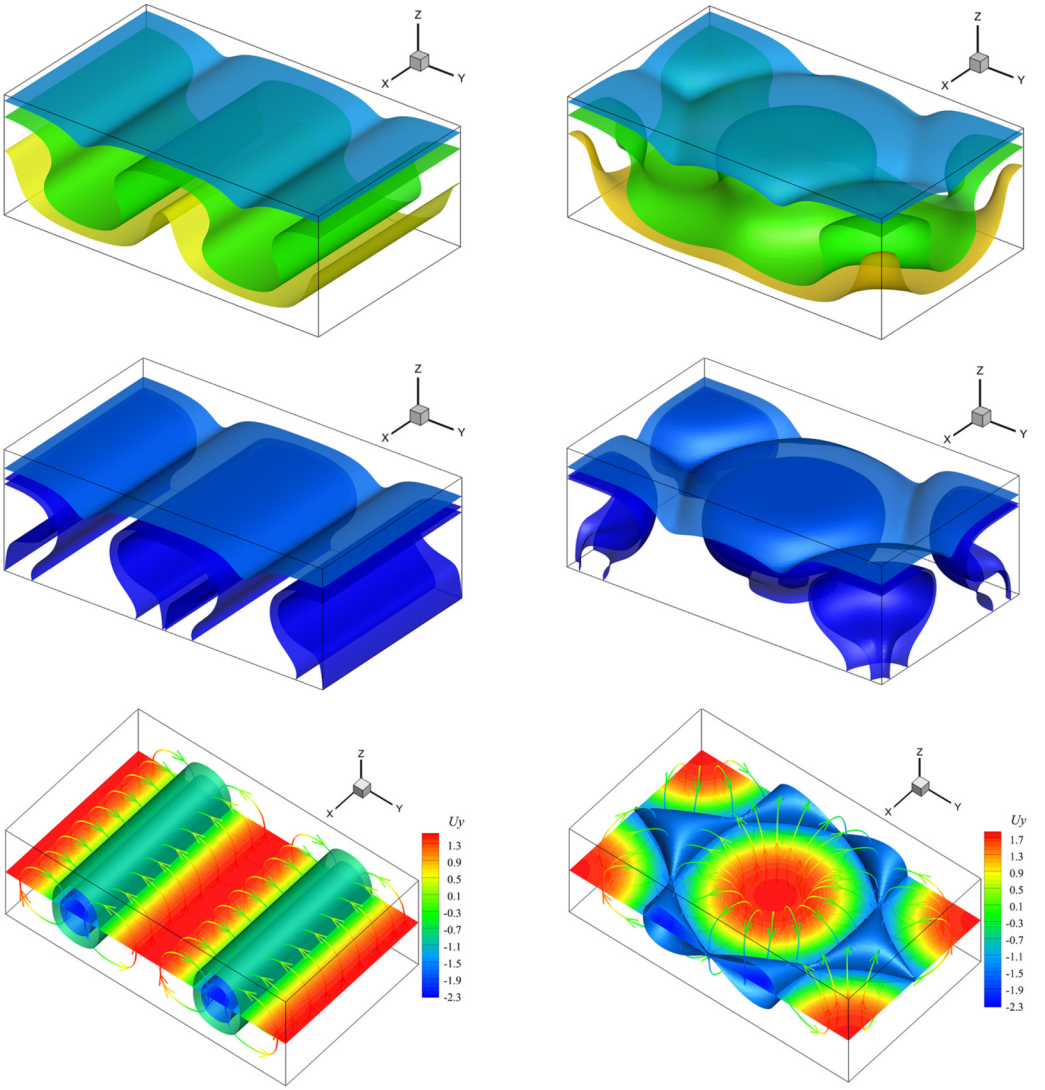

FIG. 8. The final steady results for (a) the rolls pattern and (b) the hexagonal pattern at $T = 120$, Ra $=$ 1200. From top to bottom: temperature isosurfaces for $\theta = 0.15$, 0.5, and 0.75; charge density isosurfaces for $q = 0.04$, 0.07, 0.2; a vertical velocity w slice at $y = 0.5$ with streamlines and isosurfaces.

The flow structure of the hexagonal pattern is more complicated, as seen in Fig. 8(b). The flow shows two complete hexagonal cells, with one in the center and the other separately located at the four corners. In addition, vase-shape regions free of charge, which are mutually independent of each other, appear in the centers of each convective cell. The fluid always ascends and descends in the central regions and the peripheral regions of the convective annular cells, respectively. Therefore, free charges are injected from the top electrode and move mainly with the combined velocity $K\mathbf{E} + \mathbf{u}$ in the outer region of the vase, before finally discharging at the lower collecting electrode.

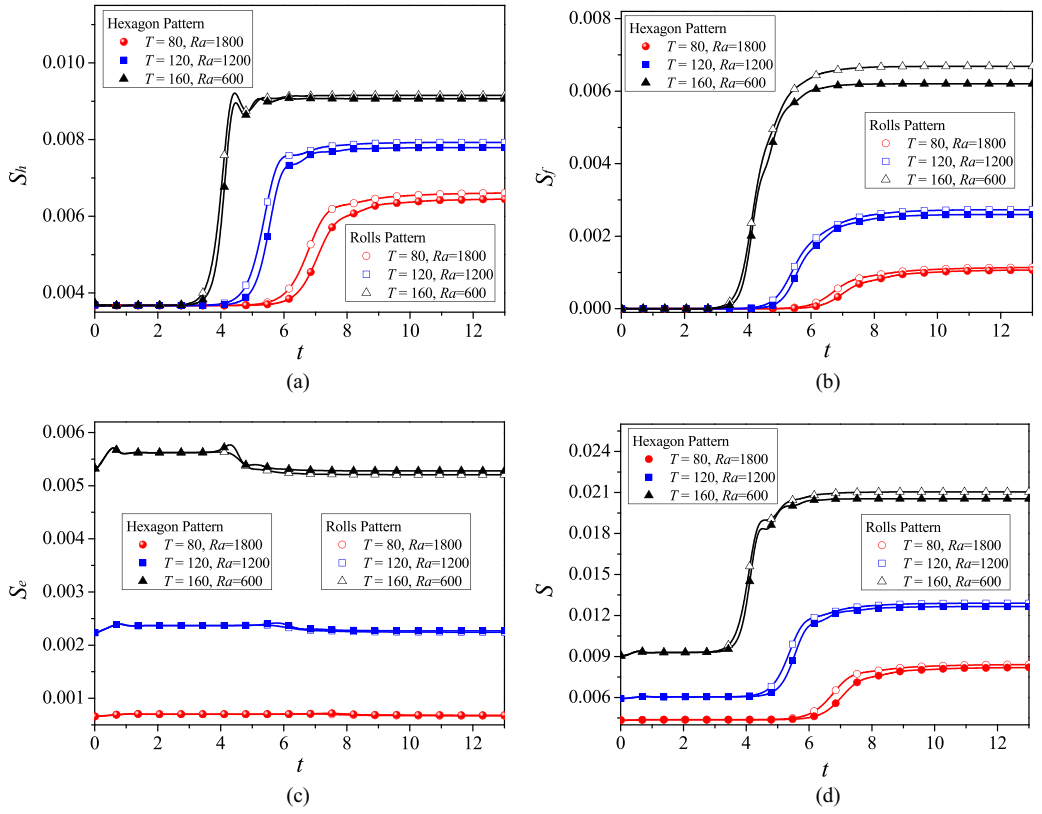

FIG. 9. The time evolution of the nondimensional entropy generation of both the rolls pattern and the hexagonal pattern for three combinations of (Ra, T): entropy generation due to (a) heat transfer, (b) fluid friction, (c) electric current, and (d) total entropy generation.

D. Entropy analysis of the cells patterns in ETC

In traditional analysis of ETC flows, quantities such as temperature, velocity, and charge density are frequently considered, but entropy properties are seldom involved. For a typical dissipative structure like this, it is to be expected that entropy analysis can provide a unique perspective on the estimation of relatively stable ETC flow patterns.

The entropy analysis and pattern selection of an ETC flow are analogous to those of a classical RBC flow. The selection of a pattern in an RBC flow, whether polygon or rolls, is a rather subtle matter, and very small alterations in the physical conditions can result in radical changes in the structure of the convection pattern. The appearance of a steady-state pattern is determined by multiple factors, including the values of nondimensional parameters (Ra and Pr), boundary and initial conditions, and the temperature dependence of physical parameters. But ETC flows are even more complex than RBC flows due to the nonlinear character of the electrical equations. Here we use entropy analysis to judge the "relative stability" of various stable solutions. It is expected that a stable solution will produce more entropy per unit time from the mean temperature field of any other solution than it does from its own mean field [52].

Figures 9(a)–9(d) present the transient evolution of entropy generation due to the irreversibility of heat transfer S_h, fluid friction S_f, and electric current S_e, as well as the total entropy generation S. Three representative cases at ($T = 80$, Ra $= 1800$), ($T = 120$, Ra $= 1200$), and ($T = 160$, Ra $= 600$) are considered for $C = 10$, $M = 10$, Pr $= 10$, and $\alpha = 10^{-4}$. In each case, both the rolls and

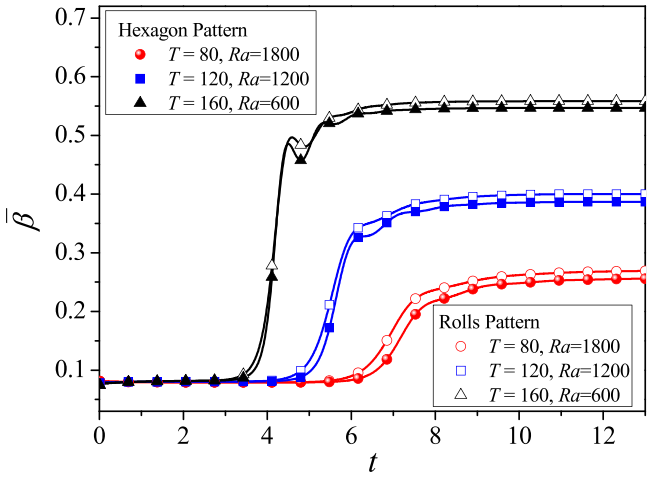

FIG. 10. A comparison of the mean-square gradient between the rolls and hexagons can be used to determine which pattern is more stable.

hexagonal patterns are motivated by the corresponding special initial perturbations. It is seen that the values of S_h and S_f for the rolls are larger than those for the hexagons in all cases, but the hexagonal pattern is generally associated with greater electrical entropy generation as shown in Fig. 9(c). The total entropy generation of the rolls pattern is larger than that of the hexagonal pattern. Therefore, we can say that the rolls are more stable than the hexagons under this simulation condition. Figure 10 shows a comparison of the mean-square gradient $\bar{\beta}$ results for the rolls and hexagons. It is seen that the time history of $\bar{\beta}$ has the same trend as for the entropy generation, confirming that the rolls are more stable than the hexagons in this case.

IV. CONCLUSIONS

In this work, a comprehensive study has been conducted to investigate the formation of a dissipative structures in a 3D electro-thermo-convective (ETC) flow. Multiple methods, from theoretical analysis to numerical simulations, have been adopted to cooperatively explain the ETC flow patterns. Linear stability analysis was conducted to determine the stability criteria (T_c and Ra_c) and critical wave numbers (k_c). To demonstrate the transient evolution of the initial perturbation and the steady-state ETC flow pattern, a numerical simulation was performed by solving the fully coupled governing equations. Furthermore, hexagonal pattern analysis and entropy generation analysis were also implemented to explore the basic features of the hexagonal cell flow pattern.

A large domain simulation ($\Gamma_x = \Gamma_y = 20$) with a random initial infinitesimal perturbation was first conducted to reproduce the realistic conditions of Atten and Lacroix's classic electrohydrodynamics experiment. The results showed that electro-convection with a random perturbation first grows into a rolls pattern, then partially breaks up into polygons, and finally evolves into a regular hexagonal pattern after a long period of evolution. The simulation showed good qualitative agreement with the experiment. Linear stability analysis was then performed to test the onset of ETC instability. By calculating the eigenvalues, we could estimate whether a given perturbation of wave number k would grow or decay. In this manner, a neutral stability curve for the ETC flow in the Ra-T plane was plotted. Good agreement was observed between the numerically predicted linear stability criteria and the modal-stability analysis.

A regular ETC hexagonal pattern was obtained in a periodic domain under a special initial perturbation. Thermal plumes in the temperature field and vase-shaped charge void regions in the charge density distribution could be readily seen. The fluid was seen to always ascend in the central

regions and descend in the peripheral regions of convective annular cells. The LBM simulation results were consistent with the analytical solutions for the hexagonal pattern in three representative planes. Besides, using entropy generation analysis, we found that the total entropy generation and mean-square temperature gradient of the rolls pattern is always larger than those of the hexagon, indicating that the rolls pattern is relatively stable under the simulation condition of a periodic cell with specific perturbation.

ACKNOWLEDGMENTS

This work was supported by the National Natural Science Foundation of China (Grants No. 51906051 and No. 52076055). and partially by financial support from the Fundamental Research Funds for the Central Universities (Grants No. FRFCU5710094020 and No. AUGA5710094020).

The data that support the findings of this study are available from the corresponding author upon reasonable request.

APPENDIX A: AN ANALYTICAL DESCRIPTION OF THE HEXAGONAL CELLS

Using linear stability analysis, we can see the onset of instability as characterized by the most unstable mode with wave number k. But a given $k = \sqrt{\alpha^2 + \beta^2}$ corresponds to infinite combinations of (α, β). Incorporating the symmetry and periodicity of the system, rolls and hexagons are the most frequently observed flow patterns in both RBC and EC problems. As the rolls flow pattern has been thoroughly discussed in relation to 2D studies, here we focus on the analysis of steady-state hexagonal cell flows.

In the study of 3D RBC, Chandrasekhar derived an analytical solution for the hexagonal pattern [2]. Here we introduce this analytical solution into the study of the ETC flow,

$$w = \frac{1}{3}W(z)\left\{2\cos\frac{2\pi}{L\sqrt{3}}x\cos\frac{2\pi}{3L}y + \cos\frac{4\pi}{3L}y\right\}, \tag{A1}$$

in which $k = 4\pi/3L$ is the wave number and L is the side length of the hexagon. Two alternative forms of Eq. (A1) can be given as [2]

$$w = \frac{1}{3}W(z)\left\{\cos\frac{4\pi}{3L}\left(\frac{\sqrt{3}}{2}x + \frac{1}{2}y\right) + \cos\frac{4\pi}{3L}\left(\frac{\sqrt{3}}{2}x - \frac{1}{2}y\right) + \cos\frac{4\pi}{3L}y\right\}, \tag{A2a}$$

$$w = \frac{1}{3}W(z)\left\{4\cos\frac{2\pi}{3L}\left(\frac{\sqrt{3}}{2}x + \frac{1}{2}y\right)\cos\frac{2\pi}{3L}\left(\frac{\sqrt{3}}{2}x - \frac{1}{2}y\right)\cos\frac{2\pi}{3L}y - 1\right\}. \tag{A2b}$$

We can now check the symmetry and periodicity of the hexagonal pattern, letting $x = \varpi\cos\vartheta$, $y = \varpi\sin\vartheta$, and substituting into Eq. (A2a) [2],

$$w = \frac{1}{3}W(z)\left\{\cos\left[\frac{4\pi\varpi}{3L}\sin(\vartheta + 60^\circ)\right] + \cos\left[\frac{4\pi\varpi}{3L}\sin(\vartheta + 120^\circ)\right] + \cos\left[\frac{4\pi\varpi}{3L}\sin\vartheta\right]\right\}. \tag{A3}$$

In Eq. (A3), we have $w(\varpi, \vartheta) = w(\varpi, \vartheta + 60^\circ)$, and using this invariance for rotation by 60°, we can prove the symmetry of the hexagonal pattern. Furthermore, the periodicity of the pattern in both the x and y directions can easily be observed from Eq. (A1), and thus

$$w(x + n\sqrt{3}L, y + 3mL) \equiv w(x, y), \tag{A4}$$

where n and m are integers. The wavelengths in the x and y directions are $L_x = \sqrt{3}L$ and $L_y = 3L$, respectively.

Expressing u and v in terms of two functions φ and ψ in the manner

$$u = \frac{\partial\varphi}{\partial x} - \frac{\partial\psi}{\partial y} \text{ and } v = \frac{\partial\varphi}{\partial y} + \frac{\partial\psi}{\partial x} \tag{A5}$$

and combining with the continuity equation $\partial u/\partial x + \partial v/\partial y + \partial w/\partial z = 0$, we have

$$\frac{\partial w}{\partial z} = -\frac{\partial u}{\partial x} - \frac{\partial v}{\partial y} \text{ and } \eta = \frac{\partial v}{\partial x} - \frac{\partial u}{\partial y}, \tag{A6}$$

where η is the z component of the vorticity used in Sec. II B. Using the spatial derivative of Eq. (A6), we have

$$\frac{\partial^2 w}{\partial z \partial x} + \frac{\partial \eta}{\partial y} = -\frac{\partial^2 u}{\partial x^2} - \frac{\partial^2 u}{\partial y^2}, \quad \frac{\partial^2 w}{\partial z \partial y} - \frac{\partial \eta}{\partial x} = -\frac{\partial^2 v}{\partial x^2} - \frac{\partial^2 v}{\partial y^2}. \tag{A7}$$

Due to the periodicity of u and v, we have $\partial^2 u/\partial x^2 + \partial^2 u/\partial y^2 = -k^2 u$ and $\partial^2 v/\partial x^2 + \partial^2 v/\partial y^2 = -k^2 u$. Besides, when marginal conditions prevail, the z component of the vorticity vanishes [2], i.e., $\nabla \eta = 0$. Then,

$$u = \frac{1}{k^2}\frac{\partial^2 w}{\partial z \partial x} = -\frac{DW}{3k^2}\frac{4\pi}{L\sqrt{3}} \sin \frac{2\pi}{L\sqrt{3}} x \cos \frac{2\pi}{3L} y, \tag{A8}$$

$$v = \frac{1}{k^2}\frac{\partial^2 w}{\partial z \partial y} = -\frac{DW}{3k^2}\frac{4\pi}{3L}\left(\cos \frac{2\pi}{L\sqrt{3}} x + 2\cos \frac{2\pi}{3L} y\right) \sin \frac{2\pi}{3L} y. \tag{A9}$$

The flow in an arbitrary vertical plane is complicated, but there are two relatively simple cases in the planes $x = 0$ and $y = 0$. Using Eqs. (A1), (A8), and (A9),

$$\begin{aligned} u &= 0, \\ v &= -\frac{DW}{3k^2}\frac{4\pi}{3L}\left(1 + 2\cos \frac{2\pi}{3L} y\right) \sin \frac{2\pi}{3L} y \qquad \text{(in the plane } x = 0\text{)}, \\ w &= \frac{1}{3} W \left(2\cos \frac{2\pi}{3L} y + \cos \frac{4\pi}{3L} y\right) \end{aligned} \tag{A10}$$

and

$$\begin{aligned} u &= -\frac{DW}{3k^2}\frac{4\pi}{\sqrt{3}L} \sin \frac{2\pi}{\sqrt{3}L} x, \\ v &= 0 \qquad \text{(in the plane } y = 0\text{)}, \\ w &= \frac{1}{3} W \left(2\cos \frac{2\pi}{\sqrt{3}L} x + 1\right). \end{aligned} \tag{A11}$$

Equations (A1), (A10), and (A11) are analytical solutions of velocity of the hexagon at specific planes.

APPENDIX B: LINEAR STABILITY ANALYSIS OF AN ETC FLOW

To study dissipative structures formation in an ETC flow, we start from an initial field that represents a stationary state of the system. After undergoing infinitesimal disturbances, only some components of the wave-number spectrum of the convective disturbance grow. Using linear stability analysis, we can determine the most unstable mode and the corresponding critical wave number, which may provide some guidance for the simulation.

The variables can be written as a summation of the base state (denoted by an overbar) and the perturbation (denoted by a prime), i.e., $\mathbf{u} = \bar{\mathbf{u}} + \mathbf{u}'$, $\hat{p} = \bar{P} + P'$, $\mathbf{E} = \bar{\mathbf{E}} + \mathbf{E}'$, $q = \bar{q} + q'$, $\phi = \bar{\phi} + \phi'$, $\theta = \bar{\theta} + \theta'$ [41]. Substituting these decomposed variables into Eqs. (1)–(5), subtracting the governing equations for the base state, and removing the high-order small quantities, leaving only the first-order term, the linear perturbation equation can be

obtained [24,34]:

$$\nabla \cdot \mathbf{u}' = 0, \tag{B1}$$

$$\frac{\partial \mathbf{u}'}{\partial t} + (\mathbf{u}' \cdot \nabla)\bar{\mathbf{u}} + (\bar{\mathbf{u}} \cdot \nabla)\mathbf{u}' = -\nabla P' + \frac{M^2}{T}\nabla^2 \mathbf{u}' + CM^2(q'\bar{\mathbf{E}} + \bar{q}\mathbf{E}') + \frac{M^4 \mathrm{Ra}}{T^2 \mathrm{Pr}}\theta' \mathbf{e}_z, \tag{B2}$$

$$\nabla^2 \phi' = -Cq', \ \mathbf{E}' = -\nabla \phi', \tag{B3}$$

$$\frac{\partial q'}{\partial t} + \nabla \cdot [(\bar{\mathbf{E}} + \bar{\mathbf{u}})q' + (\mathbf{E}' + \mathbf{u}')\bar{q} - \alpha \nabla q'] = 0, \tag{B4}$$

$$\frac{\partial \theta'}{\partial t} + \mathbf{u}' \cdot \nabla \theta' = \frac{M^2}{T\mathrm{Pr}}\nabla^2 \theta'. \tag{B5}$$

The boundary conditions for the perturbation equation are

$$\phi|_{z=0,1} = 0, \quad q|_{z=1} = 0, \ \partial q/\partial z|_{z=0} = 0, \quad \mathbf{u}|_{z=0,1} = 0, \quad \theta|_{z=0,1} = 0. \tag{B6}$$

The base states are only functions of the z direction, $\bar{\mathbf{u}} = \bar{u}(z)\mathbf{e}_z$, $\bar{\mathbf{E}} = \bar{E}(z)$, $\bar{q} = \bar{q}(z)$, $\bar{\phi} = \bar{\phi}(z)$, $\bar{\theta} = \bar{\theta}(z)$, and can be regarded as hydrostatic solution of different fields at $\alpha = 0$,

$$\bar{u} = 0, \tag{B7}$$

$$\bar{E} = a\sqrt{z+b}, \quad \bar{q} = \frac{a}{2}\frac{1}{\sqrt{z+b}} \ \bar{\phi} = -\frac{2}{3}a(z+b)^{3/2} + c, \tag{B8}$$

$$\bar{\theta} = 1 - z, \tag{B9}$$

where a, b, c are three constants dependent on the injection strength C,

$$\frac{2}{3}a[(1+b)^{3/2} - b^{3/2}] = 1, \quad b = \frac{a^2}{4C^2}, \quad c = 1 + \frac{2}{3}ab^{3/2}. \tag{B10}$$

As the pressure cannot be directly obtained, we eliminate the pressure P' by introducing the wall vorticity $\eta' = \partial_x v' - \partial_y u'$. After some simple transformation, we have [34]

$$\frac{\partial \nabla^2 w'}{\partial t} = \left[-\bar{u}\frac{\partial}{\partial x}\nabla^2 + \bar{u}_{zz}\frac{\partial}{\partial x} + \frac{M^2}{T}\nabla^4\right]w' + M^2\left[\bar{\phi}_z\left(\nabla^2 - \frac{\partial^2}{\partial z^2}\right)\nabla^2\phi' - \bar{\phi}_{zzz}\left(\nabla^2 - \frac{\partial^2}{\partial z^2}\right)\phi'\right] + \frac{M^4 \mathrm{Ra}}{T^2 \mathrm{Pr}}\left(\nabla^2 - \frac{\partial^2}{\partial z^2}\right)\theta', \tag{B11}$$

$$\frac{\partial \eta'}{\partial t} = -\bar{u}\frac{\partial}{\partial x}\eta' - \bar{u}_z\frac{\partial w'}{\partial y} + \frac{M^2}{T}\nabla^2 \eta', \tag{B12}$$

$$\frac{\partial \nabla^2 \phi'}{\partial t} = \frac{\partial \nabla^2 \phi'}{\partial z}\bar{\phi}_z + \bar{\phi}_{zzz}\frac{\partial \phi'}{\partial z} + 2\bar{\phi}_{zz}\nabla^2 \phi' - \bar{u}\frac{\partial \nabla^2 \phi'}{\partial x} - \bar{\phi}_{zzz}w' + \alpha \nabla^4 \phi', \tag{B13}$$

$$\frac{\partial \theta'}{\partial t} = -w'\frac{\partial \bar{\theta}}{\partial z} + \left(-\bar{u}\frac{\partial}{\partial x} + \frac{M^2}{T\mathrm{Pr}}\nabla^2\right)\theta', \tag{B14}$$

where the subscript z stands for the spatial derivative along the z direction.

The above equation can be written in a more compact form [24],

$$\mathbf{A}\frac{\partial \boldsymbol{\gamma}}{\partial t} = \mathbf{B}\boldsymbol{\gamma} \rightarrow \frac{\partial \boldsymbol{\gamma}}{\partial t} = \mathbf{L}\boldsymbol{\gamma}, \tag{B15}$$

where $\boldsymbol{\gamma} = [v', \eta', \phi', \theta']^T$ is the vector form of the variables to be solved. $\mathbf{A}$ and $\mathbf{B}$ are coefficient obtained from Eqs. (B11)–(B14); $\mathbf{L} = \mathbf{A}^{-1}\mathbf{B}$ represents the linearized NS operator for the ETC flow.

Under the wavelike assumption [24], the flow variables can be written as

$$f(x, y, z, t) = \hat{f}(z, t)\exp(i\alpha x + i\beta y) = \hat{f}(z)\exp(-i\omega t)\exp(i\alpha x + i\beta y), \tag{B16}$$

in which α and β are the real-valued streamwise and spanwise wave numbers. and the complex-valued ω is the circular frequency of the perturbation, with its real part ω_r representing the phase speed and its imaginary part ω_i representing the growth rate of the linear perturbation. Substituting Eq. (22) into Eq. (21), we have [24]

$$-i\omega\tilde{\boldsymbol{\gamma}} = L\tilde{\boldsymbol{\gamma}}, \tag{B17}$$

where $-i\omega$ is the eigenvalue and $\tilde{\boldsymbol{\gamma}}$ is the corresponding eigenvector.

[1] I. Prigogine and I. Stengers, *The End of Certainty* (Simon and Schuster, New York, 1997) .

[2] S. Chandrasekhar, *Hydrodynamic and Hydromagnetic Stability, Dover edition* (Dover, New York, 1981).

[3] P. Atten and J. C. Lacroix, Electrohydrodynamic stability of liquids subjected to unipolar injection: Non linear phenomena, J. Electrostat. **5**, 439 (1978).

[4] A. V. Getling, *Rayleigh-Bénard Convection: Structures and Dynamics* (World Scientific, Singapore, 1998), Vol. 11.

[5] E. Bodenschatz, W. Pesch, and G. Ahlers, Recent developments in Rayleigh-Bénard convection, Annu. Rev. Fluid Mech. **32**, 709 (2000).

[6] P. H. Traoré, A. T. PéRez, D. Koulova, and H. Romat, Numerical modelling of finite-amplitude electro-thermo-convection in a dielectric liquid layer subjected to both unipolar injection and temperature gradient, J. Fluid Mech. **658**, 279 (2010).

[7] A. Pérez, P. Vázquez, J. Wu, and P. Traoré, Electrohydrodynamic linear stability analysis of dielectric liquids subjected to unipolar injection in a rectangular enclosure with rigid sidewalls, J. Fluid Mech. **758**, 586 (2014).

[8] K. Luo, J. Wu, T. A. Pérez, H. L. Yi, and H. P. Tan, Stability analysis of electro-convection with a solid-liquid interface via lattice Boltzmann method, Phys. Rev. Fluids **4**, 083702 (2019).

[9] A. Castellanos, *Electrohydrodynamics* (Springer, New York, 1998), Vol. 380.

[10] A. Kourmatzis and J. S. Shrimpton, Turbulent three-dimensional dielectric electrohydrodynamic convection between two plates, J. Fluid Mech. **696**, 228 (2012).

[11] J. Wu, P. Traoré, A. T. Pérez, and M. Zhang, Numerical analysis of the subcritical feature of electro-thermo-convection in a plane layer of dielectric liquid, Phys. D (Amsterdam, Neth.) **311**, 45 (2015).

[12] J. Wu, P. Traoré, A. T. Pérez, and P. A. Vázquez, On two-dimensional finite amplitude electro-convection in a dielectric liquid induced by a strong unipolar injection, J. Electrostat. **74**, 85 (2015).

[13] P. H. G. Allen and T. G. Karayiannis, Electrohydrodynamic enhancement of heat transfer and fluid flow, Heat Recovery Syst. CHP **15**, 389 (1995).

[14] J. E. Bryan and J. Seyed-Yagoobi, Heat transport enhancement of monogroove heat pipe with electrohydrodynamic pumping, J. Thermo. Heat Trans. **11**, 454 (1997).

[15] J. Cotton, A. J. Robinson, M. Shoukri, and J. S. Chang, A two-phase flow pattern map for annular channels under a DC applied voltage and the application to electrohydrodynamic convective boiling analysis, Int. J. Heat Mass Transfer **48**, 5563 (2005).

[16] W. Grassi and D. Testi, A new hydrodynamic approach for jet impingement boiling CHF, Int. Commun. Heat Mass Transfer **104**, 83 (2019).

[17] Y. Guan, R. S. Vaddi, A. Aliseda, and I. Novosselov, Experimental and numerical investigation of electrohydrodynamic flow in a point-to-ring corona discharge, Phys. Rev. Fluids **3**, 043701 (2018).

[18] S. Rashidi, H. Bafekr, R. Masoodi, and E. M. Languri, EHD in thermal energy systems - A review of the applications, modelling, and experiments, J. Electrostat. **90**, 1 (2017).

[19] W. Hassen, M. I. Elkhazen, P. Traore, and M. N. Borjini, Numerical study of the electro–thermo-convection in an annular dielectric layer subjected to a partial unipolar injection, Int. J. Heat Fluid Flow **50**, 201 (2014).

[20] K. Dantchi, T. Philippe, and R. Hubert, Numerical study of the heat transfer and electro-thermo-convective flow patterns in dielectric liquid layer subjected to unipolar injection, J. Electrostat. **71**, 970 (2013).
[21] P. A. Vázquez, A. T. Pérez, P. Traoré, and J. Wu, Electroconvection in a dielectric liquid between two concentric half-cylinders with rigid walls: Linear and nonlinear analysis, Phys. Rev. E **97**, 023106 (2018).
[22] M. Talmor and J. Seyed-Yagoobi, Numerical study of micro-scale EHD conduction pumping: The effect of pump orientation and flow inertia on heterocharge layer morphology and flow distribution control, J. Electrostat. **111**, 103548 (2021).
[23] V. K. Patel, J. Seyed-Yagoobi, F. Robinson, and J. R. Didion, Effect of gravity on electrohydrodynamic conduction driven liquid film flow boiling, J. Thermophys. Heat Transfer **30**, 429 (2015).
[24] M. Zhang, F. Martinelli, J. Wu, Peter J. Schmid, and M. Quadrio, Modal and non-modal stability analysis of electrohydrodynamic flow with and without cross-flow, J. Fluid Mech. **770**, 319 (2015).
[25] M. Zhang, Weakly nonlinear stability analysis of subcritical electrohydrodynamic flow subject to strong unipolar injection, J. Fluid Mech. **792**, 328 (2016).
[26] Y. H. Diao, Y. Liu, J. Zhang, L. Guo, Y. H. Zhao, and S. Wang, Effect of electric field on the enhanced heat transfer characteristic of an evaporator with multilayered sintered copper mesh, J. Electrostat. **73**, 26 (2015).
[27] P. Traoré and A. T. Pérez, Two-dimensional numerical analysis of electroconvection in a dielectric liquid subjected to strong unipolar injection, Phys. Fluids **24**, 037102 (2012).
[28] K. Luo, J. Wu, H. L. Yi, and H. P. Tan, Lattice Boltzmann model for Coulomb-driven flows in dielectric liquids, Phys. Rev. E **93**, 023309 (2016).
[29] K. Luo, J. Wu, H. L. Yi, and H.-P. Tan, Three-dimensional finite amplitude electroconvection in dielectric liquids, Phys. Fluids **30**, 023602 (2018).
[30] K. Luo, J. Wu, H. L. Yi, and H.-P. Tan, Numerical investigation of heat transfer enhancement in electro-thermo-convection in a square enclosure with an inner circular cylinder, Int. J. Heat Mass Transfer **113**, 1070 (2017).
[31] W. J. Worraker and A. T. Richardson, The effect of temperature-induced variations in charge carrier mobility on a stationary electrohydrodynamic instability, J. Fluid Mech. **93**, 29 (2006).
[32] F. Pontiga and A. Castellanos, Physical mechanisms of instability in a liquid layer subjected to an electric field and a thermal gradient, Phys. Fluids **6**, 1684 (1994).
[33] A. V. Taraut and B. L. Smorodin, Electroconvection in the presence of autonomous unipolar injection and residual conductivity, J. Exp. Theor. Phys. **115**, 361 (2012).
[34] X. He and M. Zhang, On the flow instability under thermal and electric fields: A linear analysis, Eur. J. Mech. B. Fluids **88**, 34 (2021).
[35] Z. G. Su, T. F. Li, K. Luo, and H. L. Yi, Nonlinear behavior of electrohydrodynamic flow in viscoelastic fluids, Phys. Rev. Fluids **6**, 093701 (2021).
[36] D. Testi, Heat transfer enhancement by an impinging ionic jet in a viscous transformer coolant, Int. Commun. Heat Mass Transfer **91**, 256 (2018).
[37] M. Gao, P. Cheng, and X. Quan, An experimental investigation on effects of an electric field on bubble growth on a small heater in pool boiling, Int. J. Heat Mass Transfer **67**, 984 (2013).
[38] D. Nakhla, E. Thompson, B. Lacroix, and J. S. Cotton, Measurement of heat transfer enhancement in melting of n-Octadecane under gravitational and electrohydrodynamics (EHD) forces, J. Electrostat. **92**, 31 (2018).
[39] Z. Sun, Y. Zhang, K. Luo, A. T. Pérez, H. L. Yi, and J. Wu, Experimental investigation on melting heat transfer of an organic material under electric field, Exp. Therm. Fluid Sci. **131**, 110530 (2022).
[40] L. Wang, Y. Zhao, X. Yang, B. Shi, and Z. Chai, A lattice Boltzmann analysis of the conjugate natural convection in a square enclosure with a circular cylinder, Appl. Math. Modell. **71**, 31 (2019).
[41] Y. Guan, J. Riley, and I. Novosselov, Three-dimensional electroconvective vortices in cross flow, Phys. Rev. E **101**, 033103 (2020).
[42] A. Castellanos, Coulomb-driven convection in electrohydrodynamics, IEEE Trans. Electr. Insul. **26**, 1201 (1991).
[43] P. Atten, Electrohydrodynamic instability and motion induced by injected space charge in insulating liquids, IEEE Trans. Dielectr. Electr. Insul. **3**, 1 (1996).

[44] K. Luo, J. Wu, H. L. Yi, and H. P. Tan, Lattice Boltzmann modelling of electro-thermo-convection in a planar layer of dielectric liquid subjected to unipolar injection and thermal gradient, Int. J. Heat Mass Transfer **103**, 832 (2016).
[45] L. Wang, Z. Wei, T. Li, Z. Chai, and B. Shi, A lattice Boltzmann modelling of electrohydrodynamic conduction phenomenon in dielectric liquids, Appl. Math. Modell. **95**, 361 (2021).
[46] K. He, Z. Chai, L. Wang, B. Ma, and B. Shi, Numerical investigation of electro–thermo-convection with a solid–liquid interface via the lattice Boltzmann method, Phys. Fluids **33**, 037128 (2021).
[47] Y. Guan and I. Novosselov, Two relaxation time lattice Boltzmann method coupled to fast Fourier transform Poisson solver: Application to electroconvective flow, J. Comput. Phys. **397**, 108830 (2019).
[48] Y. Guan and I. Novosselov, Numerical analysis of electroconvection in cross-flow with unipolar charge injection, Phys. Rev. Fluids **4**, 103701 (2019).
[49] Y. Qian, D. d'Humières, and P. Lallemand, Lattice BGK models for Navier-Stokes equation, Europhys. Lett. **17**, 479 (1992).
[50] A. Castellanos, Entropy production and the temperature equation in electrohydrodynamics, IEEE Trans. Dielectr. Electr. Insul. **10**, 22 (2003).
[51] A. Bejan, *Entropy Generation through Heat and Fluid Flow* (Wiley, New York, 1982), Vol. 1.
[52] W. V. R. Malkus and G. Veronis, Finite amplitude cellular convection, J. Fluid Mech. **4**, 225 (1958).
[53] K. Luo, J. Wu, H. L. Yi, L. H. Liu, and H.-P. Tan, Hexagonal convection patterns and their evolutionary scenarios in electroconvection induced by a strong unipolar injection, Phys. Rev. Fluids **3**, 053702 (2018).